The effect of non-uniform damping on flutter in axial flow and energy-harvesting strategies

By Kiran Singh*, Sébastien Michelin and Emmanuel de Langre

LadHyX – Department of Mechanics, École Polytechnique, 91128 Palaiseau, France

The problem of energy harvesting from flutter instabilities in flexible slender structures in axial flows is considered. In a recent study, we used a reduced-order theoretical model of such a system to demonstrate the feasibility for harvesting energy from these structures. Following this preliminary study, we now consider a continuous fluid-structure system. Energy harvesting is modelled as strain-based damping, and the slender structure under investigation lies in a moderate fluid loading range, for which the flexible structure may be destabilized by damping. The key goal of this work is to analyse the effect of damping distribution and intensity on the amount of energy harvested by the system. The numerical results indeed suggest that non-uniform damping distributions may significantly improve the power-harvesting capacity of the system. For low-damping levels, clustered dampers at the position of peak curvature are shown to be optimal. Conversely for higher damping, harvesters distributed over the whole structure are more effective.

Keywords: energy harvesting; fluid–structure interactions; flutter instability; slender body theory

1. Introduction

Increasing energy demands motivate the interest in energy-harvesting concepts, where the idea is to harness the energy of naturally occurring phenomena. At the scale of kilowatts, concepts include energy harvesting from tidal currents (Westwood 2004) and ocean waves (Falcao 2010). At the lower end of the power spectrum, concepts based on photo/thermovoltaics and magneto/piezoelectrics show the scope for powering sensors and mobile electronic devices (Anton & Sodano 2007); these include energy scavenging from ambient vibrations in structures such as buildings and bridges as well as oscillatory motion of wheels in automobiles or turbines in engines (Paradiso & Starner 2005; Khaligh *et al.* 2010). Energy harvesting from fluid–structure interactions (FSIs) includes concepts such as vortex-induced vibrations (VIVs) of bluff bodies in cross-flow (Bernitsas *et al.* 2008; Grouthier *et al.* 2012), resonant vibrations induced in aerofoils mounted on elastic supports (Peng & Zhu 2009; Erturk *et al.* 2010), flutter of flexible plates (Tang *et al.* 2009; Doaré & Michelin 2011; Bryant & Garcia 2011) and

*Author and address for correspondence: OCCAM, The Mathematical Institute, 24-29 St Giles, Oxford OX13LB, UK (kiran.singh@cantab.net).

3620

combinations thereof, as for the coupled VIV–flutter energy harvester examined by Li *et al.* (2011). In this work, we focus on energy-harvesting from flutter instabilities of slender structures in an axial flow.

The classical description of flutter instabilities is self-sustained oscillations that arise owing to the unstable coupling of fluid dynamic pressure and structural bending modes, whereas for undamped structures the critical speed at flutter onset depends on fluid as well as structural properties (Païdoussis 2004). Flutter instabilities are observed in a diversity of configurations, which may be broadly classified as internal or external flows (Païdoussis 1998, 2004). Internal flow instabilities are observed in flexible pipes and channels, and are invariably motivated by biological phenomena such as flow-induced oscillations in airways and veins (Larose & Grotberg 1997; Carpenter & Pedley 2003). The pipe-conveying fluid is a canonical problem that yields deep insights into FSI; in particular, Doaré & de Langre (2006) examined the relationship between local and global instabilities and showed that locally stable configurations may become unstable owing to wave reflections at finite boundaries; this destabilizing mechanism was recently predicted for compliant channels as well (Stewart *et al.* 2009). External-flow-based instabilities include flapping flags (Alben & Shelley 2008; Eloy *et al.* 2008; Michelin *et al.* 2008) and panels (Crighton & Oswell 1991) in a steady flow. For all aspect ratios, the plate can become unstable owing to fluid loading, defined as the ratio of fluid and structure inertia, and may be represented as a non-dimensional length (Howell *et al.* 2009) or mass ratio (Eloy *et al.* 2007). Païdoussis *et al.* (2002) and more recently de Langre *et al.* (2007) examined the occurrence of instabilities in slender structures. They used experimental and theoretical techniques to examine the role of inviscid and viscous drag on static and dynamic instabilities that arise in flexible cylinders in axial flow. For a recent review on the flutter dynamics of flexible bodies in external flow, the reader is referred to Shelley & Zhang (2011) and references therein.

In this work, we analyse the scope for harvesting energy in slender elastic cantilevered structures that flutter in a steady flow. From the point of view of the fluid–solid system, energy harvesters are essentially an energy sink; therefore, for the theoretical approach adopted here, they are modelled as internal damping in the structure. As a first step, we examined the feasibility of this concept using a nonlinear model of a reduced-order system, consisting of a slender cylinder pair connected by discrete springs and dampers (Singh *et al.* 2012). It was shown that the optimal configuration for this two-degree-of-freedom system is one with energy harvesters positioned away from the instability source; such a configuration maintains self-sustained flapping in the presence of structural damping.

In this work, we generalize this approach for a continuous system, and seek to maximize energy harvesting through carefully tailored distributions of structural damping. Conventionally, structural instabilities are stabilized by damping (Larose & Grotberg 1997; Gad-el Hak 2003). However, damping may be destabilizing under moderate to heavy fluid loading conditions, as observed in infinite plates (Peake 2001), flags (Doaré & Michelin 2011) and fluid-conveying pipes (Doaré 2010). Singh *et al.* (2012) show that energy-harvesting requires the presence of two traditionally competitive elements: flutter oscillations and damping. A configuration for which flutter is destabilized by damping is especially interesting from an energy-harvesting perspective. This idea has been exploited for piezoelectric-based energy harvesting from
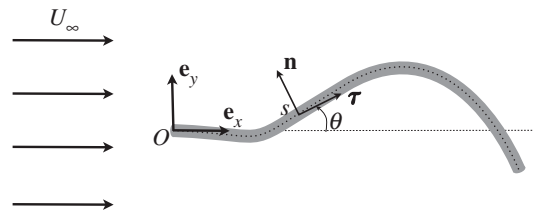
Figure 1. Slender cantilevered structure placed in a steady axial flow of velocity $U_\infty \mathbf{e}_x$ and fixed in O. The instantaneous deformation of the inextensible beam is measured by the tangent angle $\theta(s, t)$ with respect to $\mathbf{e}_x$ of the local tangent $\boldsymbol{\tau}$.

flapping flags: Doaré & Michelin (2011) used linear theory to show the gain in conversion efficiency for flags with high fluid loading destabilized by piezoelectric-based damping. In this work, we explore this idea using a general model for structural damping (equivalently energy harvesting) and a nonlinear model of the fluid structure interaction of a slender structure in a mean flow.

It is worth noting that existing insights on damping are generally based on the assumption of a constant distribution of damping in the structure (Tang *et al.* 2009), while little is known about how non-uniform damping distributions affect the dynamics. In this work, we seek clarity on the role of damping distribution on the flutter response of slender structures. The specific motivation is to identify physical mechanisms that maximize this dissipated (i.e. harvested) power.

This study is organized as follows: in §2, the model used for the dynamics of slender structures with non-uniform damping in an axial flow is presented. In §3, the case of uniform damping is considered as a reference configuration, and the role of fluid loading on destabilization by damping is discussed. Computations are then performed for a neutrally buoyant slender cylinder with moderate fluid loading, and the role of damping on the harvested power and flutter response is examined. Section 4 investigates non-uniform damping distributions and seeks optimals on two different families of damping functions, either distributed over the whole structure or focused on a particular region. In §5, the impact of damping distribution on the flutter dynamics is investigated further to understand the fundamental difference between optimal configurations at low and intermediate damping.

2. Fluid–solid model

We consider a cantilevered (clamped-free, fixed at O) slender structure of length L with crosswise dimension D, density ρ_s, stiffness B and non-uniform structural damping $B^*(s)$. The slender solid is immersed in a stream of fluid of density ρ moving at mean speed U_∞, and the solid motion is confined to the $(\mathbf{e}_x, \mathbf{e}_y)$ plane (figure 1). The equations of motion are non-dimensionalized by the characteristic system scales: ρ, L, U_∞.

(a) Nonlinear beam model

The flexible structure is modelled as an inextensible Euler–Bernoulli beam, where $\mathbf{r}(s)$ is the position vector in the fixed coordinate system $(\mathbf{e}_x, \mathbf{e}_y)$ and s is

the curvilinear coordinate. At each point along the beam, the orientation $\theta(s, t)$ is defined as the angle of the tangent vector $\boldsymbol{\tau}(s)$ with the horizontal; $\mathbf{n}(s)$ is the local normal. The nonlinear equation of motion for the beam subjected to a fluid force, $\mathbf{f}$, is

$$\frac{1}{M^*}\frac{\partial^2 \mathbf{r}}{\partial t^2} = \frac{\partial}{\partial s}\left\{\nu\boldsymbol{\tau} - \frac{1}{M^* U^{*2}}\left[\frac{\partial^2 \theta}{\partial s^2} + \frac{\partial}{\partial s}\left(\xi(s)\frac{\partial^2 \theta}{\partial s\partial t}\right)\right]\mathbf{n}\right\} + \mathbf{f}, \tag{2.1}$$

where the internal tension, $\nu(s, t)$, is essentially a Lagrange multiplier to satisfy the inextensibility condition $\partial \mathbf{r}/\partial s = \boldsymbol{\tau}$, and $\xi(s) = U_\infty B^*(s)/(BL)$ is the non-dimensional damping distribution. A Kelvin–Voigt damping model is considered here, generalizing previous contributions (Païdoussis 2004; Tang *et al.* 2009; Doaré 2010; Eloy *et al.* 2012) to non-uniform damping distributions.

The clamped-free boundary conditions must also be satisfied, namely at the fixed end ($s = 0$)

$$\theta = 0 \quad \text{and} \quad \mathbf{r} = 0, \tag{2.2}$$

and at the free end ($s = 1$)

$$\frac{\partial \theta}{\partial s} + \xi\frac{\partial^2 \theta}{\partial s\partial t} = 0, \quad \frac{\partial^2 \theta}{\partial s^2} + \frac{\partial}{\partial s}\left(\xi\frac{\partial^2 \theta}{\partial s\partial t}\right) = 0 \quad \text{and} \quad \nu = 0. \tag{2.3}$$

Consistently with prior work (Eloy *et al.* 2007; Michelin *et al.* 2008), the non-dimensional mass ratio (M^*) and flow speed (U^*) are defined as

$$M^* = \frac{\rho D L}{\rho_s A} \quad \text{and} \quad U^* = U_\infty L \left(\frac{\rho_s A}{B}\right)^{1/2}, \tag{2.4}$$

with A the cross-sectional area of the structure.

(b) Fluid dynamic model

In the limit of slender structures ($D \ll L$), and for purely potential flow upstream of the structure's trailing edge, Lighthill's large amplitude elongated-body theory (Lighthill 1971) provides a leading-order expression for the 'reactive' force $\mathbf{f}^i$ applied by the flow on the flapping body, associated with the local transverse motion of each cross section

$$\mathbf{f}^i = -\frac{m_a}{M^*}\left(\frac{\partial(u_n\mathbf{n})}{\partial t} - \frac{\partial(u_n u_\tau \mathbf{n})}{\partial s} + \frac{1}{2}\frac{\partial(u_n^2 \boldsymbol{\tau})}{\partial s}\right), \tag{2.5}$$

where $u_\tau \boldsymbol{\tau} + u_n \mathbf{n} = \partial \mathbf{r}/\partial t - \mathbf{e}_x$ is the solid's local velocity relative to the incoming flow, and $m_a = M_a/\rho_s A$, where M_a is the dimensional added mass per unit length of the cross section. Candelier *et al.* (2011) showed that Lighthill's theory compares well with Reynolds-averaged Navier–Stokes simulations to compute the forces on a swimming fish during transient manoeuvres. This reactive force does not include any flow separation associated with the transverse motion of each cross section, and, as emphasized in Candelier *et al.* (2011), for freely flapping bodies, an additional contribution for the fluid force must be included to account

for such dissipative effects. Here, an empirical 'resistive' force model is therefore added following Taylor (1952) and Eloy *et al.* (2012):

$$\mathbf{f}^v = -1/2\, C_D\, u_n |u_n| \mathbf{n}, \tag{2.6}$$

where C_D is the empirical drag coefficient, and $C_D = 1$ is used in the following for circular cross sections (Singh *et al.* 2012, for a discussion of the impact of this coefficient on the flapping dynamics). Boyer *et al.* (2008) tuned the drag coefficients to show a good agreement with direct numerical simulations.

Thus, the fluid force, $\mathbf{f}$, in equation (2.1) is modelled as the sum of the reactive ($\mathbf{f}^i$) and resistive ($\mathbf{f}^v$) components. In the remainder of the study, we assume a neutrally buoyant circular cylinder; therefore $\rho = \rho_s$ and $A = \pi D^2/4$. Unless otherwise stated, we assume $D/L = 0.1$.

Note that the fluid force description is purely local here, and does not explicitly account for wake effects. When the slender body assumption is not verified, and in particular, in the case of two-dimensional plates, an explicit description becomes necessary (Alben & Shelley 2008; Michelin *et al.* 2008; Singh & Pedley 2012).

(c) Energy harvester model

As noted earlier, energy harvesting is represented as a strain-based damping $\xi(s)$. We focus here on the mean non-dimensional harvested power:

$$\mathcal{P} = \frac{\mathscr{P}}{\rho D L U_\infty^3} = \frac{1}{M^* U^{*2}} \int_0^1 \xi(s) \langle \dot{\kappa}^2 \rangle \, ds, \tag{2.7}$$

where $\mathscr{P}$ is the mean dimensional harvested power, $\dot{\kappa}$ is the time derivative of the local curvature κ and $\langle \cdot \rangle$ is the time average taken over a period T of the limit-cycle oscillation. $\mathcal{P}$ can also be understood as the efficiency of the system.

As discussed in §1, the presence of structural damping can affect the flutter response. The intensity and distribution of damping are characterized by

$$\xi_0 = \int_0^1 \xi(s) \, ds \quad \text{and} \quad \tilde{\xi}(s) = \frac{\xi(s)}{\xi_0}. \tag{2.8}$$

Equation (2.8) allows us to independently evaluate the impact on the system response of (i) the amount of damping ξ_0 and (ii) its spatial distribution.

(d) Numerical solution

Equation (2.1) is solved numerically together with boundary conditions (2.2)–(2.3) using an iterative second-order implicit time-stepping scheme (Alben 2009), and spatial derivatives are computed using Chebyshev collocation (Boyd 2001). Conservation of energy is ensured by verifying that $\dot{E} = W_f - Q$, where

$$E = \frac{1}{2} \int_0^1 \left(\frac{|\dot{\mathbf{r}}|^2}{M^*} + \frac{\kappa^2}{M^* U^{*2}} \right) ds \tag{2.9}$$

and

$$Q = \frac{1}{M^* U^{*2}} \int_0^1 \xi(s) \dot{\kappa}^2 \, ds \quad \text{and} \quad W_f = \int_0^1 \mathbf{f} \cdot \dot{\mathbf{r}} \, ds, \tag{2.10}$$
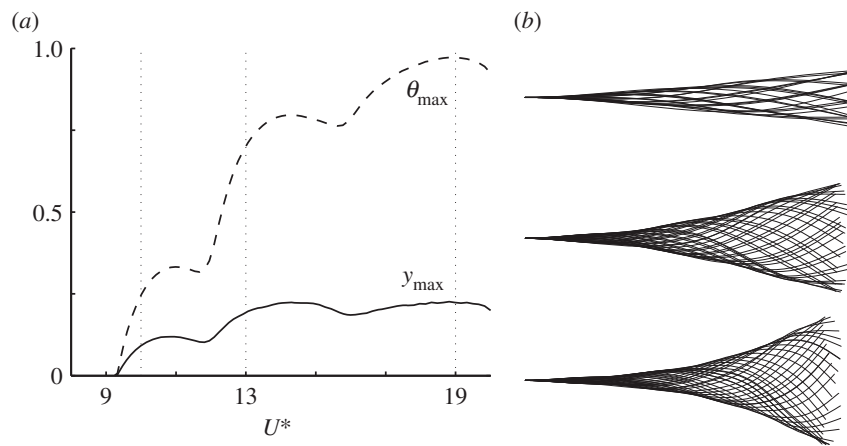
Figure 2. (*a*) Maximum deflection y_{max} (solid curve) and orientation θ_{max} (dashed curve) at the free end as a function of the non-dimensional flow velocity U^* for $M^* = 12.7$. (*b*) Snapshots of the beam response for $U^* = 10$, 13 and 19 (from top to bottom).

are respectively the mechanical energy of the system, the dissipated power and the rate of work of the fluid forces, and is classically obtained by projecting the equation of motion (2.1) on the solid velocity $\dot{\mathbf{r}}$ and by integrating over the entire beam. Also note from (2.7), $\mathcal{P} = \langle Q \rangle$. In the numerical implementation, the beam and the flow are initially at rest; the flow speed is ramped up to its steady-state value, and a small perturbation is applied to the vertical flow.

(*e*) Nonlinear response of an undamped beam

Prior to analysing the energy-harvesting properties of the system, we first examine the undamped flutter response of the structure. In figure 2, we plot the system response for increasing non-dimensional flow speed, for a circular cylinder ($M^* \approx 12.7$). The critical flow speed at which flutter ensues is verified from linear stability analysis and is confirmed with Païdoussis *et al.* (2002). Consistent with flutter in plates (Eloy *et al.* 2012), we note that this instability is a supercritical Hopf bifurcation with flow speed. The jumps in the bifurcation curve correspond to the mode switching reported in Semler *et al.* (2002); this may also be discerned from the snapshots of the beam at three different flow speeds. For the energy-harvesting computations performed in the rest of the study, we set the flow speed at $U^* = 13$, corresponding to well-developed oscillations and moderate deflections for the undamped configuration.

3. Uniform damping

Here, a uniform damping distribution $\xi(s) = \xi_0$ is considered. The dependence of critical flutter speed on the damping intensity ξ_0 is first analysed for varying values of fluid loading M^*. On the basis of these results, a moderate fluid loading is selected to study the power-harvesting capacity of the configuration.
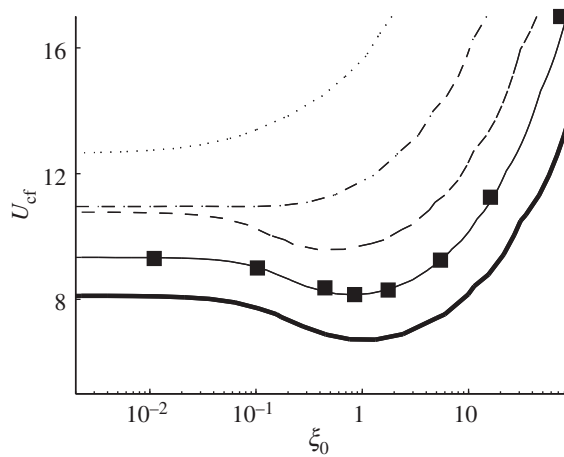
Figure 3. Variation of the critical flutter speed, U_{cf} with damping ξ_0 for $M^* = 2.5$ (dotted curve), 5.1 (dash-dotted curve), 8.5 (dashed curve), 12.7 (solid curve) and 20 (thick solid curve) obtained from linear stability analysis for uniform damping. Results of nonlinear computations for $M^* = 12.7$ are also presented (squares).

(a) Destabilization by damping: impact on critical flutter speed

As noted in §1, damping can destabilize flexible structures at sufficiently high fluid loading. Doaré (2010) shows that destabilization of long pipes with a high mass ratio is associated with a drop in the critical flutter speed. On the basis of this work, we analyse the linear stability of the system and in figure 3 compare the variation of the critical flutter speed, U_{cf}, with damping, ξ_0, at different values of fluid loading, M^*. For lightly loaded structures ($M^* < 5.5$), U_{cf} monotonically increases with damping; at higher values ($M^* \geq 8.5$), and U_{cf} decreases with damping until a specific value (ξ_m) above which U_{cf} increases rapidly; note that ξ_m increases with M^*.

For the remainder of the energy-harvesting analysis, we settle on a value of $M^* = 12.7$ (corresponding to $D/L = 0.1$): this choice allows us to analyse the scope for harvesting energy from a system at moderate fluid loading with destabilization by damping.

(b) Harvesting power with constant damping

Figure 4a presents the evolution of harvested power, $\mathcal{P}$, with damping for $10^{-3} < \xi_0 < 10$. Equation (2.7) becomes

$$\mathcal{P} = \frac{1}{M^* U^{*2}} \xi_0 \parallel \mathcal{K} \parallel_1, \tag{3.1}$$

where $\mathcal{K}(s) = \langle \dot{\kappa}^2 \rangle$ and $\parallel \mathcal{K} \parallel_1 = \int_0^1 \mathcal{K} \, ds$ is the L_1-norm of $\mathcal{K}(s)$. The evolution of the flutter response with damping is examined by plotting the re-scaled curvature term, $\bar{\mathcal{K}} = \mathcal{K}/ \parallel \mathcal{K}_0 \parallel_\infty$ (where $\mathcal{K}_0(s)$ is the value of $\mathcal{K}$ for $\xi_0 = 0$) for increasing ξ_0 (figure 4b). At small ξ_0, the response is virtually no different from the undamped case, but for $\xi_0 > 0.1$ a perceptible change is observed. First, the curvature is

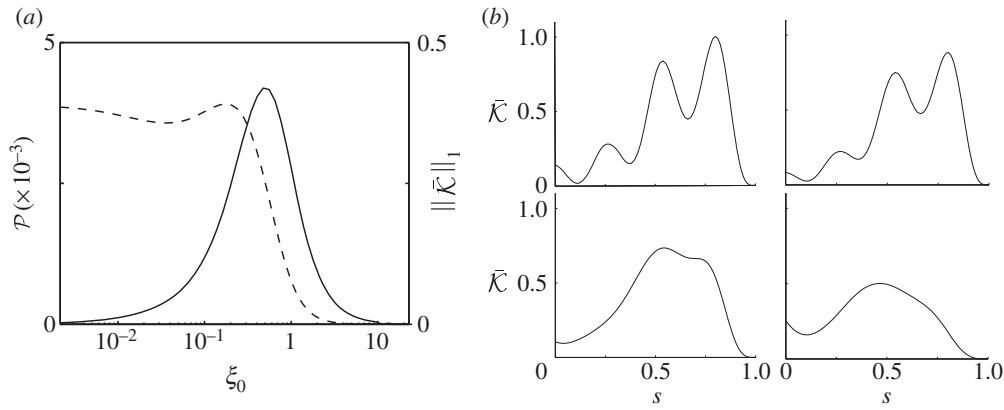Figure 4. (*a*) Evolution of the harvested power $\mathcal{P}$ (solid curve) and curvature norm $\| \bar{\mathcal{K}} \|_1$ (dashed curve) with the uniform damping intensity ξ_0. (*b*) Distribution of curvature change $\bar{\mathcal{K}}(s)$ along the beam for $\xi_0 = 0, 0.022, 0.22$ and 0.47 (from left to right and top to bottom). ($M^* = 12.7$, $U^* = 13$).

redistributed along the entire beam, and as the damping is increased further, the response of the beam is damped out globally. This can also be seen from the variation of $\| \mathcal{K} \|_1$ with ξ_0 in figure 4*a*. Notably from (3.1), it is $\| \mathcal{K} \|_1$ that directly impacts the harvested power.

As a result, for small damping, the change in system response is virtually imperceptible from the undamped case, and power simply scales linearly with ξ_0. However, damping has a strong effect on the flutter response at larger ξ_0: it reduces the amplitude of curvature change significantly and causes a sharp reduction in $\mathcal{P}$. The strategy to optimally harvest power is to find the upper bound on ξ_0 below which $\| \mathcal{K} \|_1$ can be maintained close to (or ideally enhanced above) its undamped value.

4. Non-uniform damping

The results for constant damping suggest that as long as $\| \mathcal{K} \|_1$ is maintained at undamped levels, the harvested power increases linearly with ξ_0. Figure 4*b* clearly shows that $\mathcal{K}(s)$ varies significantly along the length of the beam. Concentrating harvesters around the zone of peak curvature could therefore enhance the harvested power. This idea is tested in this section on a reduced functional space for the damping distribution $\xi(s)$. The two families of damping functions examined in §4*a* and §4*b* may be classified as dispersed and focused distributions respectively. Optimization of the harvested power is performed within each family, in anticipation of insights into the global optimal.

(*a*) *Dispersed harvester distribution*

In this section, we are interested in simple non-homogeneous distributions of damping of the form:
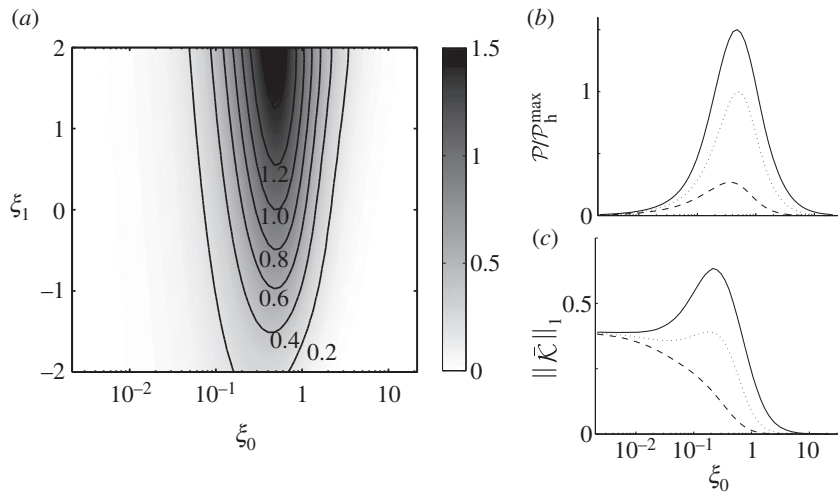
$$\xi(s) = \xi_0(1 + \xi_1(s - \tfrac{1}{2})), \tag{4.1}$$

Figure 5. Linear distribution (4.1): (*a*) re-scaled power contours $\mathcal{P}/\mathcal{P}_{\mathrm{h}}^{\max}$ for varying ξ_0 and ξ_1. (*b*) Re-scaled harvested power $\mathcal{P}/\mathcal{P}_{\mathrm{h}}^{\max}$ and (*c*) $\| \bar{\mathcal{K}} \|_1$ as a function of the damping intensity ξ_0 for linearly decreasing ($\xi_1 = -2$, dashed curve), constant ($\xi_1 = 0$, dotted curve) and linearly increasing ($\xi_1 = 2$, solid curve) damping distributions ($M^* = 12.7$, $U^* = 13$).

which are characterized by the total damping, $10^{-3} < \xi_0 < 10$, and slope, $-2 \leq \xi_1 \leq 2$. This function family corresponds to a dispersed distribution, where the damping is significant over the entire length of the structure. Figure 5*a* shows the variation of re-scaled power, $\bar{\mathcal{P}} = \mathcal{P}/\mathcal{P}_{\mathrm{h}}^{\max}$ with (ξ_0, ξ_1), where $\mathcal{P}_{\mathrm{h}}^{\max}$ is the maximum-harvested power for constant damping (§3). Figure 5 shows that for all ξ_0, the optimal distribution corresponds to $\xi_1 = 2$, when damping is distributed increasingly from fixed to free end, and that this linear distribution of damping leads to an increase of the maximum harvested power by 50 per cent compared with the uniform distribution ($\xi_1 = 0$). Through non-uniform but simple distributions of damping on the structure, it is indeed possible to enhance the flutter response above that of the undamped configuration (figure 5*c*).

(*b*) Focused harvester distribution

The results from the reduced-order analysis (Singh *et al.* 2012) suggest that the optimal distribution ought to be localized at specific points on the beam. The chief drawback of the two parameter functions examined in §4*a* is the inability to consider localized distributions of damping in specific regions. To consider such peaked distributions, we now turn to the following three-parameter family of Gaussian damping distribution:

$$\xi(s) = \xi_0 \frac{\xi_g}{\| \xi_g \|_1} \quad \text{and} \quad \xi_g = \mathrm{e}^{-\alpha(s - s_o)^2}, \tag{4.2}$$

where ξ_0 is the total damping in the system, s_o is the centre of the distribution and $1/\alpha$ is a measure of its spread in s. For increasing α, energy harvesters are increasingly concentrated around s_o.
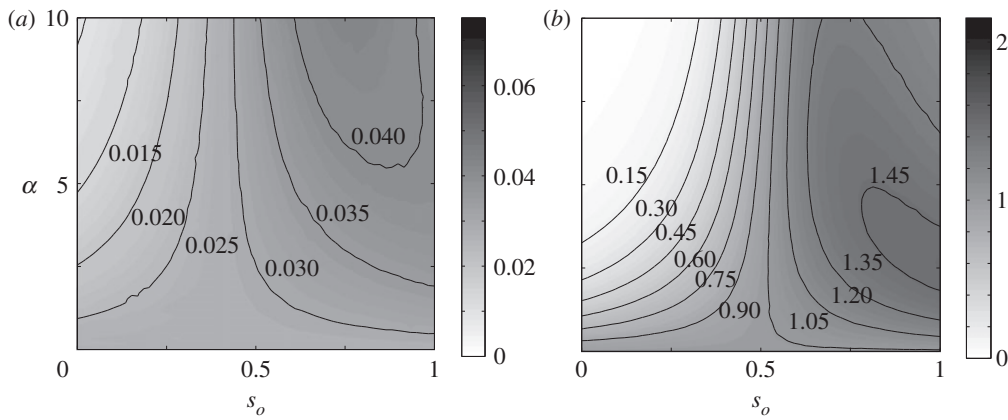
Figure 6. Gaussian distribution (4.2): maps of re-scaled power $\mathcal{P}/\mathcal{P}_\mathrm{h}^\mathrm{max}$ for varying α and s_o at (*a*) $\xi_0 = 0.01$ and (*b*) $\xi_0 = 0.47$. ($M^* = 12.7$, $U^* = 13$).
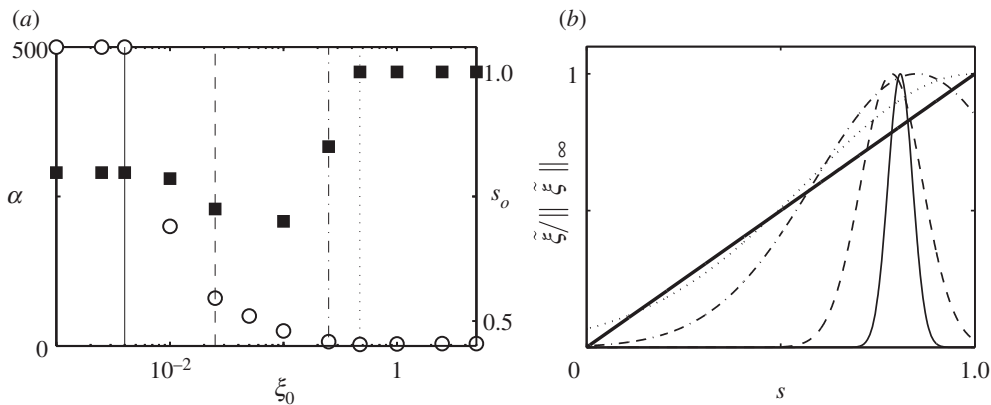

Figure 7. Gaussian function optimal configuration: (*a*) spread parameter, α, (open circles) and centre location, s_o, (filled boxes) corresponding to the optimal Gaussian distribution for a given ξ_0. (*b*) Re-scaled damping distribution at discrete $\xi_0 = 0.004, 0.025, 0.25, 0.47$ (solid, dashed, dashed-dot and dotted curves, respectively, indicated on (*a*) with vertical lines of corresponding description); superimposed is the linear optimal distribution ($\xi_1 = 2$; thick solid curve). ($M^* = 12.7$, $U^* = 13$).

Figure 6 presents the re-scaled power $\mathcal{P}/\mathcal{P}_\mathrm{h}^\mathrm{max}$ in the (α, s_o)-space for small ($\xi_0 = 0.01$) and moderate damping ($\xi_0 = 0.47$). For small damping, one sees that power is optimally harvested for dampers focused at $s_o = 0.8$, the position of the maximum of $\mathcal{K}_0$ along the beam (figure 4*b*). This is quite distinct from the high damping optimal that corresponds to a dispersed distribution ($\alpha = 2.7$, $s_o = 1$). Of particular note is that for all ξ_0, a uniform distribution ($\alpha = 0$) is preferred over a concentration of harvesters at $s_o < 0.5$.

We next examine a wider range of damping, $10^{-3} < \xi_0 < 50$, and plot the optimal values of (α, s_o), in figure 7*a*. For moderate to large damping, $\xi_0 > 0.3$, a dispersed distribution with peak at $s_o = 1$ is optimal. Conversely for $\xi_0 < 0.02$, harvesters concentrated at $s_o \approx 0.8$ (position of peak $\mathcal{K}$) is the optimal
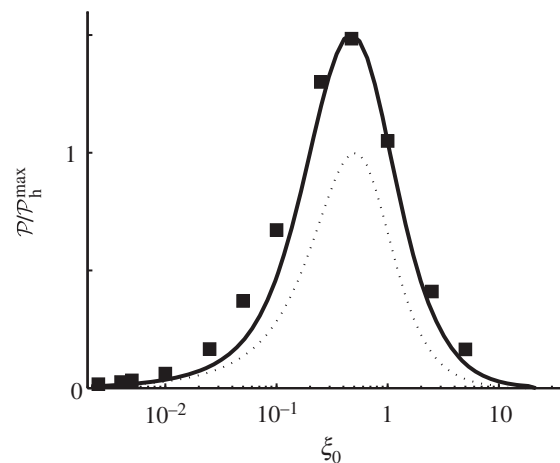
Figure 8. Optimal power values corresponding to Gaussian optimal configuration in figure 7 (squares) compared with the optimal power obtained for linear distribution ($\xi_1 = 2$; thick curve) and constant distribution ($\xi_1 = 0$; dotted curve).

configuration. Note that for these computations we set $0 < \alpha < 500$, and at these values of ξ_0 the upper bound is reached; more detailed insights and computations on the small damping regime are presented in §5. Figure 7*b* shows the evolution with ξ_0 of the optimal normalized distribution and illustrates the transition from focused to dispersed profiles when the total damping is increased.

It is possible to determine the optimal harvested power for each value of ξ_0; in figure 8, these optimals are compared with the results for uniform and linear distributions. Strikingly, the peak power values are coincident for linear and Gaussian distributions, which is consistent with the similarity in distributions (figure 7*b*). Because of the fundamentally different structures of the distribution used, this result suggests that the optimal obtained with such simple functions represents a good approximation of the absolute optimal. Departing from this maximum of harvested power, in particular at small damping, we see that concentrated harvesting is superior to the optimal linear distribution.

These results confirm that non-uniform damping distributions can be advantageously employed to enhance the power harvesting capacity. Focused damping distributions are optimal for small damping, whereas dispersed distributions are preferential at higher damping. Section 5 investigates in more detail this transition by considering the impact of damping on the nonlinear dynamical response of the system.

5. Discussion: impact of localized damping

The earlier-mentioned computations suggest a very different impact of damping on the dynamics of the structure depending on the magnitude of ξ_0, thereby leading to quite different optimal strategies to maximize the harvested power. In this section, we first consider the limit of asymptotically small damping before studying the effect of focused dampers on the body's dynamics.
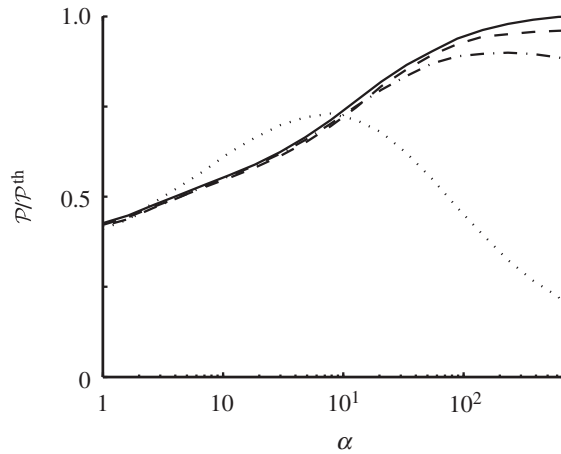
Figure 9. Focused harvesters at $s_o = 0.81$ for small damping: curves show the normalized power for increasingly focused harvesters for small damping values: $\xi_0 = 2.2 \times 10^{-5}$ (solid curve), $\xi_0 = 2.2 \times 10^{-4}$ (dashed curve), $\xi_0 = 2.2 \times 10^{-3}$ (dashed-dot curve), $\xi_0 = 2.2 \times 10^{-2}$ (dotted curve) and $M^* = 12.7$, $U^* = 13$.

(a) Optimal distribution for asymptotically small damping

For asymptotically small damping ($\| \xi \|_\infty \ll 1$, with $\| \xi \|_\infty$ the maximum value of $\xi(s)$ for $s \in [0\ 1]$), the flapping dynamics is not modified at leading order so that $\mathcal{K} = \mathcal{K}_0 + O(\| \xi \|_\infty)$. Thus

$$\mathcal{P} \sim \frac{1}{M^* U^{*2}} \int_0^1 \xi(s) \mathcal{K}_0 \, \mathrm{d}s \leq \frac{\xi_0}{M^* U^{*2}} \| \mathcal{K}_0 \|_\infty \tag{5.1}$$

and this upper bound can be approached asymptotically using, for example, the Gaussian distribution (4.2) centred on the maximum of $\mathcal{K}_0$ and increasing α. More precisely, any peaked distribution of damping of L_1-norm ξ_0 centred on this maximum and with a typical width (here $\alpha^{-1/2}$) much smaller than the length scale λ associated with the $\mathcal{K}_0$ peak width should approach the theoretical upper bound $\mathcal{P}^{\mathrm{th}} = \xi_0 \| \mathcal{K}_0 \|_\infty /(M^* U^{*2})$, provided that the maximum damping remains small enough that the approximation for $\mathcal{P}$ in equation (5.1) still holds (which in the present case is equivalent to keeping $\alpha^{1/2}\xi_0$ bounded).

This conjecture is tested numerically using a Gaussian distribution, equation (4.2), with $s_o = 0.8$, and by computing the harvested power for small damping: $2.2 \times 10^{-5} < \xi_0 < 2.2 \times 10^{-2}$. Figure 9 shows $\mathcal{P}/\mathcal{P}^{\mathrm{th}}$ and confirms that this conjecture indeed holds because for increasing α, the power asymptotically approaches its optimal for small enough ξ_0. When $\xi_0 \geq 2.2 \times 10^{-3}$, the asymptotic value $\mathcal{P}^{\mathrm{th}}$ cannot be reached any more: as α is increased, the effect of the maximum damping $\alpha^{1/2}\xi_0$ on the flutter dynamics is important even before the dampers are focused enough for $\mathcal{P}$ to approach $\mathcal{P}^{\mathrm{th}}$.

Two essential results are illustrated here. For sufficiently small damping, the nonlinear response of the structure remains unchanged; so the best strategy is to focus all the harvesters in the region of maximum curvature-change.
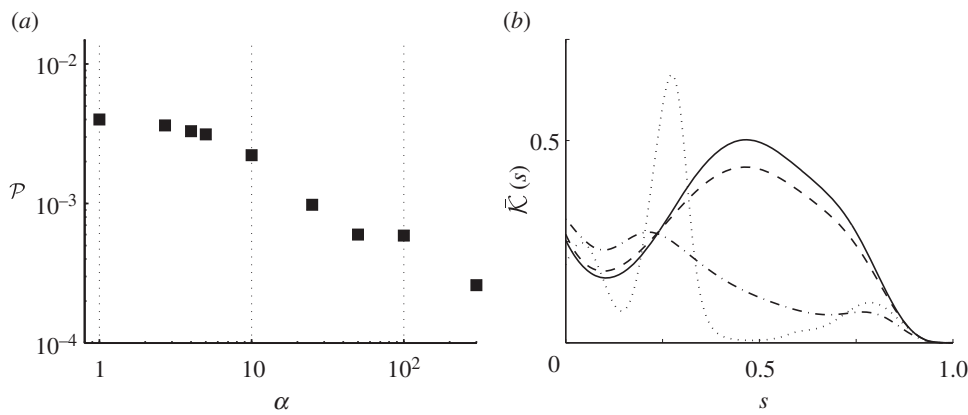
Figure 10. Focused harvesters at $s_o = 0.45$ for large damping ($\xi_0 = 0.47$): (*a*) power dependence on α and (*b*) $\bar{\mathcal{K}}(s)$ for $\alpha = 0, 1, 10, 10^2$ (solid, dashed, dashed-dot, dotted curves, respectively). ($M^* = 12.7$, $U^* = 13$).

However, finite levels of damping significantly modify the nonlinear dynamics of the beam; so at these levels, a narrow focusing of damping is sub-optimal. Next, we investigate further the behaviour at finite damping.

(*b*) *Impact of finite and localized damping*

The computations from §4 show that for Gaussian distributions and $\xi_0 > 0.02$, a defocusing of harvesters is preferable, as the system response becomes increasingly influenced by damping. In order to understand the impact on the system's response, the Gaussian distribution (4.2) is used in the high damping range and α is varied over a range that transitions the distribution from dispersed to focused ($0 < \alpha < 10^2$) with $\xi_0 = 0.47$ and $s_o = 0.45$ (corresponding to the position of $\| \mathcal{K} \|_\infty$ for $\alpha = 0$). Consistent with figure 6, the harvested power in figure 10*a* decreases with α, and figure 10*b* shows the evolution of $\mathcal{K}(s)$.

For dispersed distributions ($\alpha < 10$), $\mathcal{K}(s_o)$ decreases with α and the zone of maximum curvature-change shifts to regions of reduced damping. Nonetheless, non-zero damping in this zone is adequate to retrieve some of the energy. For $\alpha > 10$, damping becomes increasingly focused and the flexible body does not deform anymore near the damper ($\mathcal{K}(s_0) \approx 0$): no energy is harvested anymore, because no deformation occurs near the harvester's position, and this is reflected in the sharp drop in power in figure 10*b*. This illustrates the main effect of a focused distribution for finite damping: we see a redistribution of the solid's deformation to regions with little or no damping. This is also the reason why a focused damping distribution is not appropriate for optimal energy harvesting in the finite damping range.

6. Conclusions

In this work, we considered the possibility of harvesting energy from a slender body fluttering in an axial flow, and in particular, the impact of harvester distribution on the performance of the system as well as potential optimization

strategies. To this end, a simplified fluid–solid model was proposed with energy harvesting represented as non-uniform structural damping. Depending on the fluid-to-solid inertia ratio, damping can actually enhance the flutter response of the structure, as well as reduce the critical flow velocity above which the system can operate.

For uniform damping distributions, maximizing the harvested power appears as a trade-off on the damping intensity: for small damping, the flutter response is only weakly modified and the harvested power increases as more damping is added to the system. For higher damping however, the dynamical response can be strongly modified and the self-sustained oscillations are eventually mitigated. The effect of a non-uniform distribution of harvesters along the structure was considered next. We show that even simple non-uniform distributions such as linear and Gaussian functions, can lead to an increase in harvested peak power on the order of 50 per cent. The similarity in the optimal distribution and in performance obtained through an optimization on two fundamentally different families of distributions suggests that simple strategies can capture rather well the characteristics of the global optimal distribution.

Investigating further into the relationship between damping and flutter response, we showed that for small damping, localized harvesting is optimal as it takes full advantage of the system's maximum curvature without impacting its dynamics significantly. On the other hand, for finite damping, focused distributions perform rather poorly as the beam response adapts to rigidify the damped region, leading to negligible harvested power. Instead, non-uniform distributed damping over the entire length of the system becomes optimal.

Returning to the result from the simple biarticulated model (Singh *et al.* 2012), we note a clear difference in the optimal configurations. While the reduced-order model optimal has dampers focused at the fixed end, the continuous optimal requires a dispersed distribution with minimal damping at the fixed end and increasing to a maximum at the free end. However, we find a crucial difference between the two system configurations: while the biarticulated system has a single moving region of curvature (the second articulation) that is responsible for driving the instability, deformations may occur all along the length of the beam in the continuous system. Therefore, in the latter, curvature can be displaced away from regions with focused damping while still maintaining the flutter dynamics. In both cases, a careful understanding of the dynamics of the system is necessary to determine the optimal non-uniform positioning of energy harvesters.

References

Alben, S. 2009 Simulating the dynamics of flexible bodies and vortex sheets. *J. Comp. Phys.* **228**, 2587–2603. (doi:10.1016/j.jcp.2008.12.020)

Alben, S. & Shelley, M. 2008 Flapping states of a flag in an inviscid fluid: bistability and the transition to chaos. *Phys. Rev. Lett.* **100**, 074301. (doi:10.1103/PhysRevLett.100.074301)

Anton, S. & Sodano, H. 2007 A review of power harvesting using piezoelectric materials (2003–2006). *Smart Mater. Struct.* **16**, 1–21. (doi:10.1088/0964-1726/16/3/R01)

Bernitsas, M. M., Raghavan, K., Ben-Simon, Y. & Garcia, E. M. H. 2008 VIVACE (vortex induced vibration aquatic clean energy): a new concept in generation of clean and renewable energy from fluid flow. *J. Offshore Mech. Arct.* **130**, 041101. (doi:10.1115/1.2957913)

Boyd, J. 2001 *Chebyshev and Fourier spectral methods*. New York, NY: Dover Publications.

Boyer, F., Porez, M., Leroyer, A. & Visonneau, M. 2008 Fast dynamics of an eel-like robot: comparisons with Navier–Stokes simulations. *IEEE Trans. Robot.* **24**, 1274–1288. (doi:10.1109/TRO.2008.2006249)

Bryant, M. & Garcia, E. 2011 Modeling and testing of a novel aeroelastic flutter energy harvester. *J. Vib. Acoust.* **133**, 011012. (doi:10.1115/1.4002788)

Candelier, F., Boyer, F. & Leroyer, A. 2011 Three-dimensional extension of Lighthill's large-amplitude elongated-body theory of fish locomotion. *J. Fluid Mech.* **674**, 196–226. (doi:10.1017/S002211201000649X)

Carpenter, P. W. & Pedley, T. J. (eds) 2003 *IUTAM: Flow through collapsible tubes and past other highly compliant boundaries*, vol. 72, IUTAM Symposium. Dordrecht, The Netherlands: Kluwer Academic Publishers. Kluwer.

Crighton, D. G. & Oswell, J. E. 1991 Fluid loading with mean flow. (I). Response of an elastic plate to localized excitation. *Phil. Trans. R. Soc. Lond. A* **335**, 557–592. (doi:10.1098/rsta.1991.0060)

de Langre, E., Doaré, O., Païdoussis, M. P. & Modarres-Sadeghi, Y. 2007 Flutter of long flexible cylinders in axial flow. *J. Fluid Mech.* **571**, 371–389. (doi:10.1017/S002211200600317X)

Doaré, O. 2010 Dissipation effect on local and global stability of fluid-conveying pipes. *J. Sound Vib.* **329**, 72–83. (doi:10.1016/j.jsv.2009.08.029)

Doaré, O. & de Langre, E. 2006 The role of boundary conditions in the instability of one-dimensional systems. *Eur. J. Mech. B Fluids* **569**, 151–184.

Doaré, O. & Michelin, S. 2011 Piezoelectric energy harvesting from flutter instability: local/global linear stability and efficiency. *J. Fluids Struct.* **27**, 1357–1375.

Eloy, C., Souilliez, C. & Schouveiler, L. 2007 Flutter of a rectangular plate. *J. Fluids Struct.* **23**, 904–919. (doi:10.1016/j.jfluidstructs.2007.02.002)

Eloy, C., Lagrange, R., Souilliez, C. & Schouveiler, L. 2008 Aeroelastic instability of a flexible plate in a uniform flow. *J. Fluid Mech.* **611**, 97–106. (doi:10.1017/S002211200800284X)

Eloy, C., Kofman, N. & Schouveiler, L. 2012 The origin of hysteresis in the flag instability. *J. Fluid Mech.* **691**, 583–593. (doi:10.1017/jfm.2011.494)

Erturk, A., Vieira, W. G. R., De Marqui, C. & Inman, D. J. 2010 On the energy harvesting potential of piezoaeroelastic systems. *Appl. Phys. Lett.* **96**, 184103. (doi:10.1063/1.3427405)

Falcao, A. 2010 Wave energy utilization: a review of the technologies. *Renew. Sust. Energ. Rev.* **10**, 899–918. (doi:10.1016/j.rser.2009.11.003)

Gad-el Hak, M. 2003 Drag reduction using compliant walls. In *IUTAM: Flow through collapsible tubes and past other highly compliant boundaries*, vol. 72, (eds P. W. Carpenter and T. J. Pedley), pp. 191–229. Dordrecht, The Netherlands: Kluwer Academic Publishers.

Grouthier, C., Michelin, S. & de Langre, E. 2012 Energy harvesting using vortex-induced vibrations of tensioned cables. (http://arxiv.org/abs/1203.0236)

Howell, R. M., Lucey, A. D., Carpenter, P. W. & Pitman, M. W. 2009 Interaction between a cantilevered-free flexible plate and ideal flow. *J. Fluids Struct.* **25**, 544–566. (doi:10.1016/j.jfluidstructs.2008.12.004)

Khaligh, A., Zeng, P. & Zheng, C. 2010 Kinetic energy harvesting using piezoelectric and electromagnetic technologies-state of the art. *IEEE Trans. Ind. Electron.* **57**, 850–860. (doi:10.1109/TIE.2009.2024652)

Larose, P. & Grotberg, J. 1997 Flutter and long-wave instabilities in compliant channels conveying developing flows. *J. Fluid. Mech.* **331**, 37–58. (doi:10.1017/S0022112096003667)

Li, S., Yuan, J. & Lipson, H. 2011 Ambient wind energy harvesting using cross-flow fluttering. *J. Appl. Phys.* **109**, 026104. (doi:10.1063/1.3525045)

Lighthill, M. J. 1971 Large-amplitude elongated-body theory of fish locomotion. *Proc. R. Soc. Lond. B* **179**, 125–138. (doi:10.1098/rspb.1971.0085)

Michelin, S., Llewellyn Smith, S. G. & Glover, B. 2008 Vortex shedding model of a flapping flag. *J. Fluid Mech.* **617**, 1–10. (doi:10.1017/S0022112008004321)

Païdoussis, M. P. 1998 *Fluid-structure interactions: slender structures and axial flow*, vol. 1. London, UK: Academic Press.

Païdoussis, M. P. 2004 *Fluid-structure interactions: slender structures and axial flow*, vol. 2. London, UK: Academic Press.

Païdoussis, M. P., Grinevich, E., Adamovic, D. & Semler, C. 2002 Linear and nonlinear dynamics of cantilevered cylinders in axial flow. I. Physical dynamics. *J. Fluids Struct.* **16**, 691–713. (doi:10.1006/jfls.2002.0447)

Paradiso, J. A. & Starner, T. 2005 Energy scavenging for mobile and wireless electronics. *IEEE Pervas. Comput.* **4**, 18–27. (doi:10.1109/MPRV.2005.9)

Peake, N. 2001 Nonlinear stability of a fluid-loaded elastic plate with mean flow. *J. Fluid Mech.* **434**, 101–118. (doi:10.1017/S0022112001003573)

Peng, Z. & Zhu, Q. 2009 Energy harvesting through flow-induced oscillations of a foil. *Phys. Fluids* **21**, 123602. (doi:10.1063/1.3275852)

Semler, C., Lopes, J. L., Augu, N. & Païdoussis, M. 2002 Linear and nonlinear dynamics of cantilevered cylinders in axial flow, Part 3: nonlinear dynamics. *J. Fluids Struct.* **16**, 739–759. (doi:10.1006/jfls.2002.0445)

Shelley, M. & Zhang, J. 2011 Flapping and bending bodies interacting with fluid flows. *Ann. Rev. Fluid Mech.* **43**, 449–465. (doi:10.1146/annurev-fluid-121108-145456)

Singh, K. & Pedley, T. 2012 Modelling lateral manoeuvres in fish. *J. Fluid Mech.* **697**, 1–34. (doi:10.1017/jfm.2012.1)

Singh, K., Michelin, S. & de Langre, E. 2012 Energy harvesting from fluid-elastic instabilities of a cylinder. *J. Fluids Struct.* **30**, 159–172. (doi:10.1016/j.jfluidstructs.2012.01.008)

Stewart, P. S., Waters, S. L. & Jensen, O. 2009 Local and global instabilities of flow in a flexible-walled channel. *Eur. J. Mech. B Fluids* **28**, 541–557. (doi:10.1016/j.euromechflu.2009.03.002)

Tang, L., Païdoussis, M. & Jiang, J. 2009 Cantilevered flexible plates in axial flow: energy transfer and the concept of flutter-mill. *J. Sound Vib.* **326**, 263–276. (doi:10.1016/j.jsv.2009.04.041)

Taylor, G. I. 1952 Analysis of the swimming of long and narrow animals. *Proc. R. Soc. Lond. A* **214**, 158–183. (doi:10.1098/rspa.1952.0159)

Westwood, A. 2004 Ocean power: wave and tidal energy review. *Refocus* **5**, 50–55. (doi:10.1016/S1471-0846(04)00226-4)